

Revealing microcanonical phase diagrams of strongly correlated systems via time-averaged classical shadows

Gaurav Gyawali,^{1,2} Mabruur Ahmed,³ Eric Aspling,³ Luke Ellert-Beck,^{4,5} and Michael J. Lawler^{3,1,2}

¹*Department of Physics, Cornell University, Ithaca, NY 14853*

²*Department of Physics, Harvard University, Cambridge, MA 02138, USA*

³*Department of Physics, Applied Physics, and Astronomy, Binghamton University, Binghamton, NY 13902*

⁴*School of Physics and Applied Physics, Southern Illinois University, Carbondale, IL 62901*

⁵*Department of Physics, University of Rhode Island, Kingston, RI 02881*

(Dated: November 3, 2022)

Quantum computers and simulators promise to enable the study of strongly correlated quantum systems. Yet surprisingly, it is hard for them to compute ground states[Kitaev]. They can, however, efficiently compute the dynamics of closed quantum systems. We introduce time-average classical shadows(TACS) and machine learning(ML) methods to take advantage of this efficiency to study microcanonical quantum thermodynamics. Using the one-dimensional transverse field Ising model(1DTFIM), we first validate the unsupervised ML method of diffusion maps on classical shadows data from ground state calculations on 100 qubit systems. We then show that diffusion maps applied to TACS data from quantum dynamics simulations beginning from cat states show distinct phase-defining features and correctly identifies the quantum phase transition. Finally, we introduce a Bayesian inference method to compute the second Renyi entropy, a stand in for entropy, the primary thermodynamic potential of microcanonical ensemble. Our results provide evidence that quantum simulators and computers capable of outperforming classical computers at dynamics simulations can also produce quantum thermodynamic data with quantum advantage.

I. INTRODUCTION

Simulation of strongly correlated electrons in the context of quantum chemistry and condensed matter physics is one of the potential areas in which quantum computers will have a significant advantage over their classical counterparts [1–3]. Strong interaction between the ostensibly simple electrons can give rise to novel phases including high-temperature superconductivity [4, 5], strange metallic behavior[6], fractional excitations [7], and quantum spin liquids[8]. Condensed matter physics aims to understand these novel behaviors by studying their phase diagrams. However, failure of perturbation theory and exponential scaling of the Hilbert space for strongly correlated electrons presents a formidable challenge to classical simulation methods such as exact diagonalization, density matrix renormalization group(DMRG) [9–11], quantum Monte-Carlo [12] and dynamical mean-field theory[13]. Whereas, this same challenge provides an exciting opportunity for near-term quantum computers.

Harnessing the power of a quantum computer to simulate quantum systems [14] requires (i) algorithms that can be executed in a reasonable time and (ii) the ability to learn from quantum experiments without exponentially many measurements. Studying the phases via ground state preparation is a QMA-complete problem [15–18], which cannot be carried out in a reasonable time, even with quantum resources. However, performing dynamics on a quantum state is known to be a BQP-hard problem [19, 20], possible within polynomial time. Likewise, it has been shown that shadow tomography[21] methods such as classical shadows[22–24] are effective at predicting properties using very few measurements.

In classical statistical mechanics, ergodicity provides a

link between time averages and statistical averages [25]. In quantum mechanics, unitary time evolution retains memory of the initial state, so the link is different yet still enabled by equilibration of macroscopic observables. This is made possible by certain general conditions on an initial state[26–30], which allow these observables to equilibrate quickly. Thus, if we can find interesting problems and initial states for which the order parameter (a macroscopic observable that characterizes the existence of a phase) equilibrates before the qubits decohere, we can use quantum computers to perform microcanonical dynamics and study the regions of the phase diagram inaccessible via classical computing resources.

In this manuscript, we present an approach to identifying phase diagrams of strongly correlated systems via dynamics simulations on a quantum computer. It consists of i) identifying an initial state, ii) evolving this state in time using a suitable algorithm, iii) using classical shadow tomography technique to convert the quantum state to classical data, and iv) applying unsupervised machine learning methods to discover phases of matter. We illustrate it with the 1-dimensional Transverse Field Ising Model(1DTFIM).

A schematic overview of our approach is shown in Fig. 1. It consists of using diffusion maps [31, 32], an unsupervised machine learning(UL) algorithm, to machine learn phase features from unlabeled phase diagram data generated by a quantum computer. Specifically, we apply diffusion maps to CS of ground states from a 100 qubit simulation and show they successfully learn the magnetic phase transition of 1DTFIM (see section II). It does so by *discovering* the relevant parameters such as magnetization and transverse magnetic field. These results follow similar machine-learning-from-CS success stories in other

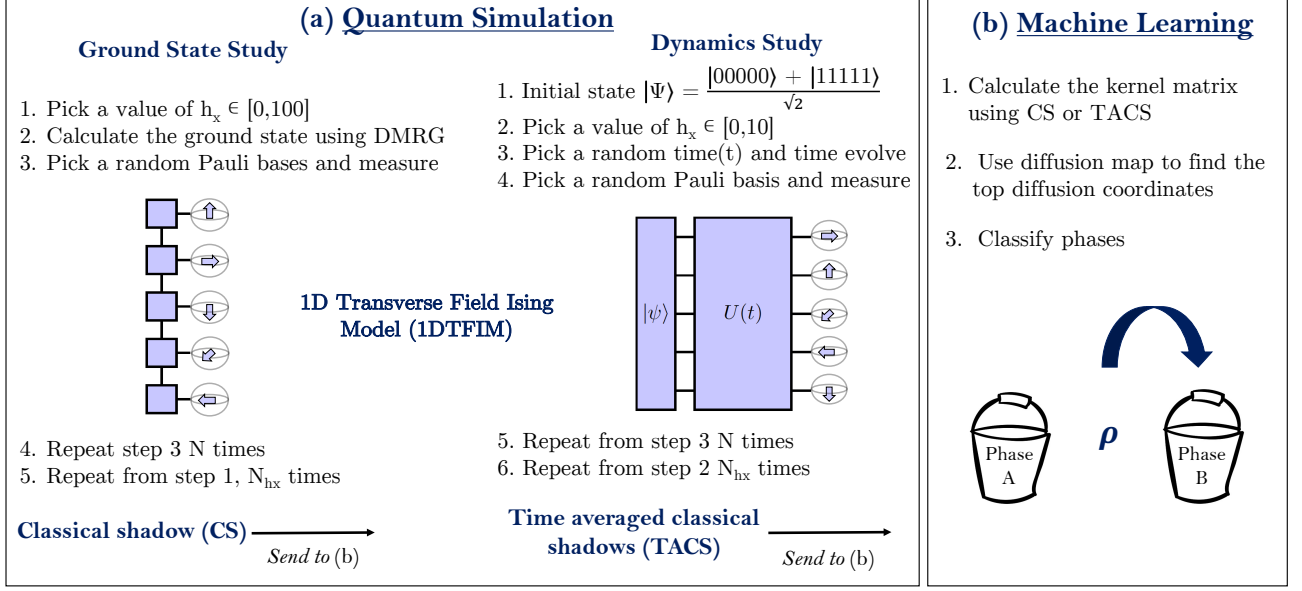


FIG. 1: Schematic overview of our study. (a) Classical shadows(CS) of ground states and time averaged classical shadows(TACS) from dynamics of a time-reversal invariant GHZ state are generated using quantum simulation. (b) The classical data from quantum simulation is then fed into diffusion map, an unsupervised machine learning algorithm to learn the phases.

contexts[22–24, 33]. We then show (section III) diffusion maps can also identify the phase transition and quantum critical region *when trained on dynamics data from just 20 qubits*. This data is in the form of a representation we introduce: time-averaged classical shadows (TACS)—a shadow tomographic[21] representation of von Neumann’s time-averaged density matrix[26]. TACS are a straightforward extension of CS to capture quantum microcanonical dynamics of finite-size finite-time quantum simulations. Our results thus validate the exciting possibility of studying the phase diagrams of strongly correlated electrons using quantum computers.

II. VON NEUMANN’S MICROCANONICAL ENSEMBLE

A central goal of quantum computing is to build qubits that are completely isolated from their environment. While this is not the case today, the current development of quantum error correction techniques[34, 35] suggests it is in our future. Simulating quantum systems on a quantum computer will therefore take place *within the microcanonical ensemble*. But quantum microcanonical dynamics, the evolution of a closed quantum system under Schrödinger’s equation, does not directly produce the microcanonical ensemble.

Following von Neumann’s 1929 paper[26, 36] on the quantum ergodic theorem, it is straightforward to derive the equilibrium distribution of a quantum system using density matrices. Assuming we start from an initial state $|\psi(0)\rangle$ and evolve under a Hamiltonian H via a quantum

circuit algorithm to $|\psi(t)\rangle$, the equilibrium distribution is captured by the time-averaged density matrix

$$\rho_T = \frac{1}{T} \int_0^T dt |\psi(t)\rangle \langle \psi(t)| \xrightarrow{T \rightarrow \infty} \omega = \sum_k P_k |\psi(0)\rangle \langle \psi(0)| P_k, \quad (1)$$

where P_k is a projector onto the k^{th} degenerate subspace of the energy eigenvalues i.e. $P_k = \sum_{n \in k} |E_n\rangle \langle E_n|$. Existence of this equilibrium density matrix ω results in the ergodic principle that long-time averages of observables should be captured by the statistical averaging with respect to ω . Specifically, in the Schrödinger picture,

$$\langle O \rangle_T = \frac{1}{T} \int_0^T dt \langle \psi(t) | O | \psi(t) \rangle \quad (2)$$

$$= \frac{1}{T} \int_0^T dt \text{Tr}(|\psi(t)\rangle \langle \psi(t)| O) \quad (3)$$

$$= \text{Tr}(\rho_T O) \xrightarrow{T \rightarrow \infty} \text{Tr}(\omega O) \quad (4)$$

Thus, the time-averaged density matrix is the link between time averages and statistical averages.

The connection to the microcanonical ensemble, obtained by quantizing the classical microcanonical ensemble, is achieved by taking the thermodynamic limit, measuring only coarse-grained observables, and requiring non-degenerate energy level spacings. Under these circumstances, von Neumann obtained

$$\omega \rightarrow \rho_{mc} = \frac{1}{\Omega} \sum_{E < E_n < E + \Delta} |E_n\rangle \langle E_n| \quad (5)$$

where all states in an energy window $[E, E + \Delta]$ are included in the sum for some window size Δ , and Ω is the phase-space volume of this constant energy shell. So ρ_T approaches ρ_{mc} in the limit of long times and large systems sizes, but for any finite T and system size, ρ_T is the actual microcanonical ensemble defined as the ensemble produced by the Schrödinger equation.

In numerics, two things are of utmost importance—reaching the thermodynamic limit and understanding the errors that may result along the way. Using the above logic, an equilibrium phase diagram with finite size errors associated with a reasonable choice of initial conditions is achievable. For each initial condition, it's possible to check whether the time series was run long enough for relevant observables to reach equilibrium (not all observables equilibrate until an exponential amount of time has passed[27, 37]). If so, the only errors remaining are of finite size and will be different for each choice of initial conditions. A family of initial conditions that all yield the same microcanonical ensemble, when scaled up, is, therefore, a key resource to study equilibrium statistical mechanics on a quantum computer. Although the equilibrium properties are independent of the initial state, the time required to reach equilibration depends on the initial state via the effective dimension given by $d_{\text{eff}} = 1/\sum p_k^2$, where $p_k = |\langle \psi | E_k \rangle|^2$. Here, p_k measures how many energy eigenstates have a significant weight in $|\psi\rangle$ and subsequently, a large effective dimension results in rapid equilibration with a bound on the equilibration time given by the second largest occupancy [27, 37]. The distribution of the p_k 's also affects equilibration times[38]. These arguments suggest we want to look for an initial state that exhibits a small overlap with most energy levels or a macroscopic occupation of a single energy level. In practice, we are concerned with the distinguishability of the time-averaged state vs. the equilibrium state in terms of experimentally relevant observables. Therefore, we need not worry about the equilibration of the full-density matrix as long as the equilibration of the relevant order parameters can be achieved.

In order to study von Neumann's microcanonical ensemble, we need to compare it to what we already know. As such, in the next section, section III, we will turn to a ground state study using the methods we will employ for our thermodynamics study to validate these methods first, before applying them to the study of TACS.

III. GROUND STATE DATA

To verify our approach to phase classification, we first apply it to ground states of the ferromagnetic 1DTFIM defined by the Hamiltonian:

$$H = - \sum_{\langle i,j \rangle} Z_i Z_j + h_x \sum_i X_i, \quad (6)$$

where $\langle . \rangle$ denotes the nearest neighbors, Z_i is the Pauli operator in the z-direction, and h_x is a parameter propor-

tional to the transverse magnetic field. At zero temperature, this model has a ferromagnetic phase for $|h_x| < 1$, and a paramagnetic phase for $|h_x| > 1$. The ground state study aims to detect the second-order phase transition at $h_x = 1$ for a 100 site 1DTFIM using diffusion maps. The ground states were generated using density matrix renormalization group (DMRG) [9–11] with ITensor package[39]. Training datasets were generated using two kinds of measurements on these ground states—(i) computational basis measurements to obtain the Z dataset and (ii) measurements on a random Pauli basis to obtain the CS dataset.

A. Classical Shadows

Obtaining any useful information from a quantum computer requires performing measurements on a quantum state, which is destructive to the quantum information by nature. Since the dimension of the Hilbert space increases exponentially in the number of qubits, a naive strategy to learn the state requires an exponentially large number of copies. Aaronson[21] introduced an alternative method using the notion of shadow tomography, an approximate classical description of the quantum state, in which M properties of a quantum state can be estimated with error ϵ by only $O(\frac{M}{\epsilon^2})$ copies of the state. We can think of a shadow as an approximation of a quantum state ρ by summing over measurement outcomes x , obtained by performing measurements on bases b for a quantum state x i.e.

$$S[\rho] = \sum_{b,x} P(b) \mathcal{P}_{b,x} \rho \mathcal{P}_{b,x}, \quad (7)$$

where $\mathcal{P}_{b,x}$ is a projector onto the measurement outcome x on basis b , and $P(b)$ is the probability of choosing b .

Based on this notion, Huang et al.[23, 24, 40] developed an algorithm called classical shadows and showed that it is highly successful at learning the properties of a many-body system. Two kinds of measurement protocols were proposed to construct classical shadows—(i) random Clifford measurements on the entire Hilbert space; (ii) random single-qubit Pauli measurements. Protocol (ii) results in very shallow measurement circuits and thus is more suitable for the NISQ-era[41] hardware. After measuring each of the qubits in some random Pauli basis X , Y or Z with outcomes ± 1 , the post-measurement wavefunction is given by the product state $|s^{(n)}\rangle = \bigotimes_{l=1}^L |s_l^{(n)}\rangle$. Here, $|s_l^{(n)}\rangle \in \{|0\rangle, |1\rangle, |+\rangle, |-\rangle, |i+\rangle, |i-\rangle\}$ is a Pauli basis state to which the l^{th} qubit has collapsed. The classical shadow $S_N[\rho]$ is obtained by summing over N such randomized measurement outcomes as follows

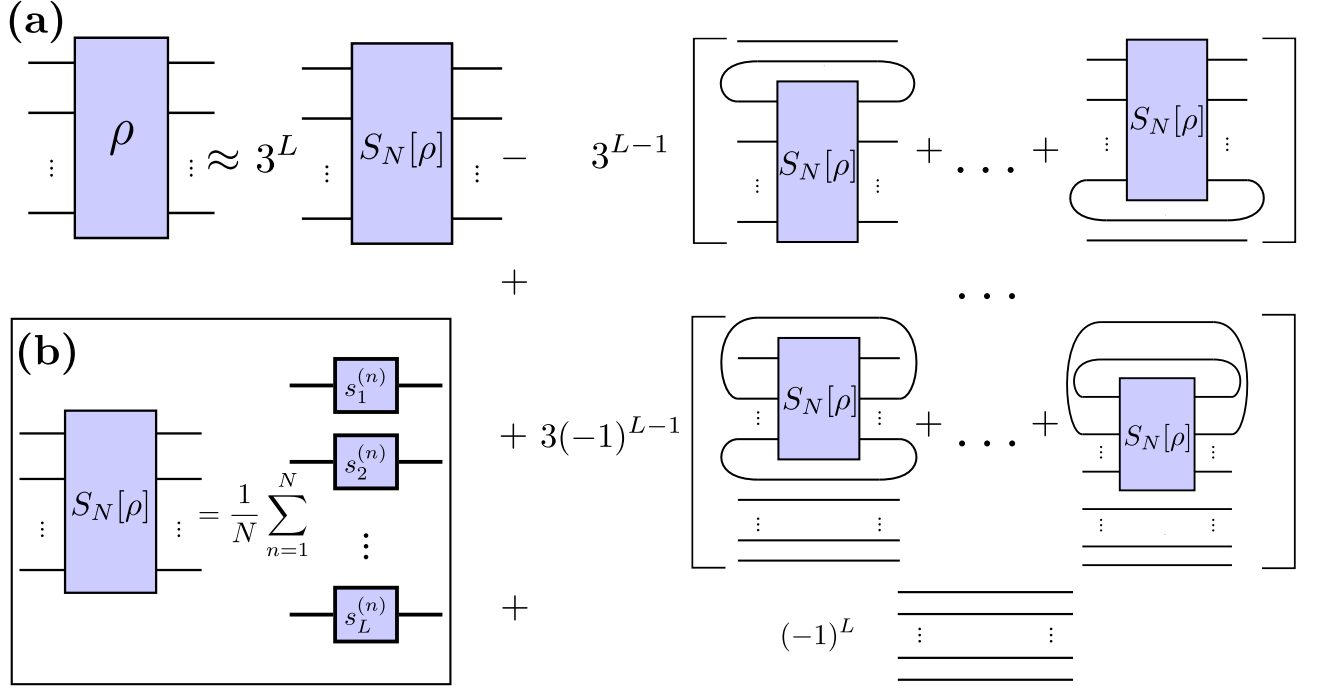


FIG. 2: Diagrammatic description of classical shadows showing a linear relationship between $S_N[\rho]$ and estimator $\sigma_N[\rho] \approx \rho$. (a) The full-density matrix ρ can be approximated by summing over reduced classical shadows with a coefficient that grows exponentially in the number of remaining qubits. (b) A classical shadow $S_N[\rho]$ is obtained by summing over N measurement outcomes on random Pauli bases. For a given N , a reduced density matrix, that involves smaller coefficients in the expansion, can be approximated more accurately compared to the full density matrix.

(also see Fig. 2(b))

$$S_N[\rho] = \frac{1}{N} \sum_{n=1}^N |s^{(n)}\rangle \langle s^{(n)}| \quad (8)$$

$$= \frac{1}{N} \sum_{n=1}^N |s_1^{(n)}\rangle \langle s_1^{(n)}| \otimes \cdots \otimes |s_L^{(n)}\rangle \langle s_L^{(n)}|. \quad (9)$$

The underlying quantum state ρ can be approximated by adding the reduced classical shadows (see Fig. 2(a)). This sum simplifies to the following expression from Ref. [23, 24, 40]

$$\rho \approx \sigma_N(\rho) = \frac{1}{N} \sum_{n=1}^N \sigma_1^{(n)} \otimes \cdots \otimes \sigma_L^{(n)}, \quad (10)$$

where

$$\sigma_l^{(n)} = 3 |s_l^{(n)}\rangle \langle s_l^{(n)}| - \mathbb{I}. \quad (11)$$

The definition of $S_N(\rho)$ presented above is different from Refs. 23 and 40 which defines it to be the dataset of shots itself and not the density matrix obtained from these shots. But both are useful for Fig. 2 shows the density matrix $S_N(\rho)$ defined above is linearly related to

the estimator $\sigma_N(\rho)$ of the quantum state ρ obtained by Refs. 23, 24, and 40. A derivation of Fig. 2 using tensor network diagrams is presented in Appendix A.

Although estimating the exact density matrix requires $N \rightarrow \infty$, we still desire to predict various linear as well as nonlinear functions of ρ (e.g., $\text{Tr}(O\rho)$ and $\text{Tr}(\rho \log(\rho))$ respectively). This can be achieved with $N \propto \log(L)4^k/\epsilon^2$ copies of the state, where k is the locality of operator O [33]. It was shown in Ref. [23] that classical machine learning algorithms can efficiently predict the ground state properties of gapped Hamiltonians in finite spatial dimensions after learning the classical shadows from a training set. An example of interest is classifying the quantum phases of matter. Classifying the symmetry-breaking phases is conceptually simple because it involves calculating $\text{tr}(\rho O)$ for some k -local observable O , such that $\text{tr}(\rho O) \geq 1 \forall \rho \in \text{phase A}$ and $\text{tr}(\rho O) \leq -1 \forall \rho \in \text{phase B}$.

In contrast to the symmetry-breaking phases, capturing continuous phase transitions involves nonlinear observables like thermodynamic potentials. These observables involve measuring a nonlinear function of ρ , for example, the entropy. Learning such nonlinear functions requires an expressive ML model. Thus, it is beneficial to devise a mapping from classical shadows to a high-dimensional feature space that includes the polynomial

expansion of many-body reduced density matrices and encapsulate this feature space in a kernel function. Using such kernels then establishes a rigorous guarantee that a classical ML model can efficiently classify nonlinear functions, phase transitions, and even topological phases of matter[23].

B. Machine Learning Method: Diffusion Maps

In this paper, we utilized unsupervised machine learning methods called diffusion maps [31, 32] to extract features from the shadows data. A diffusion map is a nonlinear dimensionality reduction technique that relies on learning the underlying manifold from which the data points have been generated. Recently, this method was used to identify phases in systems with complex order parameters, which are difficult to learn using linear methods (such as principal component analysis (PCA)[42]). Examples of such phase identification studies include; topological phases and phase transitions [43], incommensurate phases, and many-body localized phases in quantum systems [44].

In this application of diffusion maps, one can imagine a random walk on a dataset $X(x_1, x_2, \dots, x_N)$, where the x_n are estimators $\sigma_N(\rho)$ of density matrices ρ obtained from different points in the phase diagram. The transition probability $P(j|i)$ of jumping from x_i to x_j in a single ‘‘timestep’’ is proportional to the kernel function $k(x_i, x_j)$, which is a similarity measure between the two data points. Here we use the classical shadow kernel function prescribed in [23], defined to be for two points x and \tilde{x} in the dataset

$$k^{(shadow)}(x, \tilde{x}) = k^{(shadow)}(\sigma_N(\rho), \sigma_N(\tilde{\rho})) = \exp \left\{ \left(\sum_{n, n'=1}^N \frac{\tau}{N^2} \exp \left\{ \left(\frac{\gamma}{L} \sum_{l=1}^L \text{Tr} \left(\sigma_l^{(n)} \tilde{\sigma}_l^{(n')} \right) \right) \right\} \right) \right\}. \quad (12)$$

Then, we construct a transition probability matrix P such that

$$P(j|i) = \frac{k^{(shadow)}(i, j)}{\sum_l k^{(shadow)}(i, l)}. \quad (13)$$

After t timesteps of the random walk, the transition probabilities are given by the matrix P^t , where P_{ij}^t gives the probability of going from x_i to x_j in t timesteps, it's a sum of the probabilities associated with all of the possible paths to go from x_i to x_j in t timesteps. As t increases, the diffusion process unfolds, where data points situated along the overall geometric structure of the dataset become more strongly connected because of the abundance of strongly connected intermediate points along the way. The parameter ‘diffusion distance’ is defined to quantify this idea of connectivity between two data points given by

$$D_t^2(x_i, x_j)^2 = \sum_{m=1}^N |P_{im}^t - P_{jm}^t|^2 \quad (14)$$

where the bigger the diffusion distance, the weaker the connection between them. The data points are then mapped onto a new ‘diffusion space’ so that the diffusion distance in data space is equal to the Euclidean distance in this new space. It can be shown [31] that such a map can be made in the following way:

$$x_i \rightarrow y_i = [\lambda_1^t \psi_1(i), \lambda_2^t \psi_2(i), \dots, \lambda_{N-1}^t \psi_{N-1}(i)] \quad (15)$$

where λ_k and ψ_k are eigenvalues and right eigenvectors of the matrix P , $\psi_k(i)$ is the i -th element of the k -th eigenvector. ψ_k form an orthogonal set of basis vectors for the diffusion space. Then the diffusion distance is,

$$D_t^2(x_i, x_j) = |y_i - y_j|^2 = \sum_{k=1}^{N-1} \lambda_k^{2t} [\psi_k(i) - \psi_k(j)]^2 \quad (16)$$

In equations (15) and (16) the $k = 0$ component is ignored ($\psi_0(i) = \frac{1}{\sqrt{N}}$, $\lambda_0 = 1$), as it is constant for all i , hence trivial. Equation (16) suggests a dimensionality reduction, as the terms with bigger λ_k will dominate the sum increasingly as $t \rightarrow \infty$. So only the m diffusion space dimensions associated with the bigger eigenvalues ($m \ll N$) are kept. The data points are then projected onto this m -dimensional space to reveal features in the dataset.

C. Phase Classification of Ground States

For the ground state study, we used two datasets generated via two different shadow tomographies. The first (Z dataset) contains qubit measurements only along the Z-axis [in Eq. 7, $P(b) = 1$ for $b = Z$, $P(b) = 0$ for all other b]. While the other (CS-dataset) has randomized Pauli measurements using the Classical Shadows method [$P(b) = \frac{1}{3}$ for $b \in \{X, Y, Z\}$]. Both of them contain 200 100-spin 1DTFIM ground state shadows, each state for a different h_x value (h_x ranging from 0.1 to 100). Since the Z -magnetization is the order parameter for TFIM, the UL algorithm should be able to learn the phases of the model from the Z dataset. Using this knowledge, we compare the Z dataset and the CS data to see if the algorithm can successfully identify phases in it.

By deploying diffusion maps armed with the shadows kernel function (Eq. 12) as our UL model, we are able to identify the phases from both the Z data and the CS data. In both cases, we set $\tau = 1$, $\gamma = 1$ in Eq. 12. For the Z data, we chose the first five non-trivial eigenvectors as the diffusion space basis vectors because the P -matrix (Eq. 13) eigenvalue spectrum shows the first five eigenvalues to be larger than others (Fig. 3(a)). Mapping

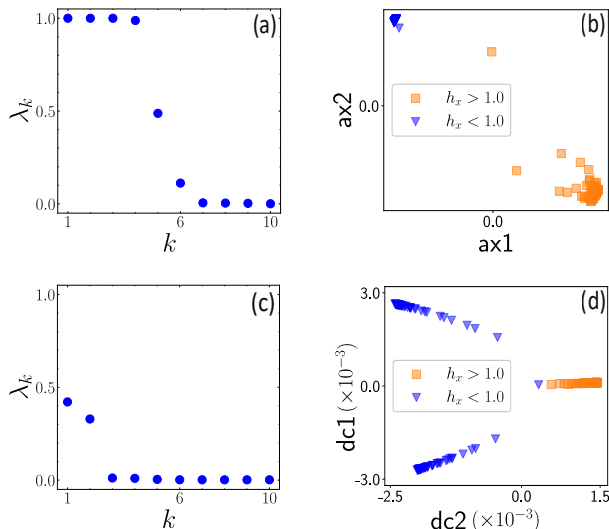


FIG. 3: Learning phases from ground state (CS and Z) data. (a) and (c) show the 10 largest eigenvalues of the P -matrix (excluding the trivial $k = 0$) for (a) Z dataset and (c) CS dataset. (b) Z datapoints in 5D diffusion space visualized in 2D, using metric MDS. Clustering clearly emerges based on the two phases of the model.

(d) CS datapoints in 2D diffusion space, the figure reveals the symmetry-breaking phase transition. In this case, there is a direct correlation of relevant parameters, the z -magnetization and the h_x -values, with machine-learned diffusion, coordinates dc1 and dc2 respectively. Notice the CS-data shows three clusters in (d), while Z-data shows only two in (b), which is a consequence of the shadow kernel function for the former is not spin-flip symmetric while that of the latter is.

the states from Z data onto this five-dimensional diffusion space, we found that clear clustering emerges based on the phases of the states. We used multidimensional scaling (MDS), a dimensionality reduction method [45] that seeks to preserve point-to-point distances, to project these states onto a 2D plane. We see a clear separation of the two phases even on this 2D reduced space (Fig. 3(b)), indicating the machine’s success in identifying the two phases.

From the CS data, the unsupervised learning algorithm was also able to learn about the phases and the underlying parameters of the model. We can see in Fig. 3(c) that the P matrix has two non-trivial eigenvalues larger than the rest. The eigenvectors corresponding to these two eigenvalues are the basis vectors of the reduced diffusion space. Figure 3(d) shows all of the ground state classical shadows projected onto this two-dimensional plane. It shows three groups- the top left and the bottom left are the all-up and all-down states, whereas the group on the center-right are states in the disordered phase. This closely resembles the spontaneous symmetry-breaking phase transition of 1DTFIM[46]. The learned diffusion

coordinates (dc1 and dc2) have direct correlations with the magnetization $\langle M_z \rangle$ and the field values h_x respectively, as shown in appendix C (Fig. 7).

The above-mentioned clustering is dependent on the number of snapshots N for a given state. However, the dimensionality reduction and the subsequent clustering will settle down after a minimum value of N has been reached (N_c). Increasing the value of N beyond that point does not change the results in any significant way, and in our case (N_c (Z data) $<$ N_c (CS data)), it should be easier for the algorithm to learn the phase space structure from the Z-data (hence fewer snapshots are required).

Despite the successful identification of the ground state phases with the CS+ML model, the fact remains that the problem of calculating ground-states is a QMA-hard problem [17]. While there is no shortage of algorithms designed to generate ground-states, the necessity of a scalable model can be better shown with a known BQP problem; revealing the microcanonical phase diagram from dynamics data.

IV. MICROCANONICAL DYNAMICS OF THE 1DTFIM

Consider now Fig. 4, the thermodynamic phase diagram of the 1DTFIM relating internal energy $E = \langle \psi(0) | \hat{H} | \psi(0) \rangle$ to the transverse magnetic field h_x . This phase diagram is relevant for a microcanonical dynamics study governed by the entropy $S(E, h_x)$. This phase diagram exists even for a simulation over a finite time T and with a finite number of spins N but with finite T , finite N errors that round the phase transitions and render the results dependent on initial conditions. We present in this figure our expectations for the phase diagram in this context, pointing out where the phase diagram will sharpen in the thermodynamic limit. We further highlight the path through the phase diagram carried out by our simulations below, showing that we expect it to cross the quantum critical region and so be sensitive to the phase diagram at a rounded level.

A. Results

With the knowledge of expected microcanonical dynamics (see Fig. 4), we now present an effective classical representation of quantum data obtained from a microcanonical dynamics on a quantum computer. Noticing that the time averaged integral amounts to an expectation value of the pure state density matrix $|\psi(t)\rangle\langle\psi(t)|$ over the probability distribution $P_T(t) = (1/T) (\Theta(T-t) - \Theta(-t))$, where $\Theta(x)$ is the Heaviside step function, we define *time averaged classical shad-*

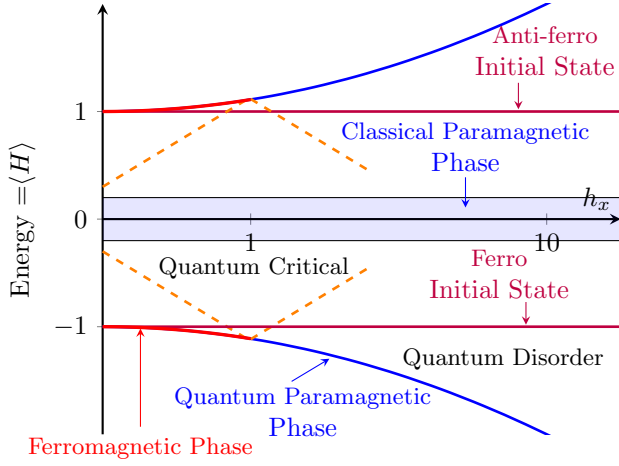


FIG. 4: A sketch of the expected 1DTFIM phase diagram at finite T and finite N as a function of internal energy E and transverse magnetic field h_x .

This diagram is a modification of the canonical ensemble representation of the phase diagram in Ref. 47, adapted to the microcanonical ensemble. The spectrum is mirror symmetric about $E = 0$ due to the chiral symmetry $\mathcal{C} = ZY ZY ZY \dots$

ows(TACS) by the map

$$TACS[\rho] = \lim_{T \rightarrow \infty} \int dt \sum_{b, \sigma} P_T(t) P(b) \mathcal{P}_{b, \sigma} |\psi(t)\rangle \langle \psi(t)| \mathcal{P}_{b, \sigma} \quad (17)$$

Hence by sampling the joint probability distribution $P_T(t)P(b)$ to obtain (t_i, b_i) , $i = 1 \dots N$, and then measuring one shot σ_i from $|\psi(t_i)\rangle$ in basis b_i we obtain a finite-shot TACS via

$$TACS_N[\rho] = \sum_{i=1}^N |t_i b_i \sigma_i\rangle \langle t_i b_i \sigma_i| \quad (18)$$

We ran quantum dynamics of 1DTFIM using the TDVP algorithm[48, 49] starting from the GHZ state $|\psi(0)\rangle = \frac{|000\dots\rangle + |111\dots\rangle}{\sqrt{2}}$ to generate TACS data from 500 randomly sampled dimensionless time values between $t = 10.0$ to $t = 20.0$ and 187 randomly sampled h_x field values between $h_x = 0.1$ to $h_x = 10.0$. For each h_x , a TACS was obtained from the $N = 500$ shots at random times over the fixed T time interval following Eq. 18. Then these 187 classical shadows were the data points with which we performed unsupervised learning by constructing the 187×187 kernel matrix using the shadow kernel in equation (12) and then using diffusion maps for dimensionality reduction. Fig. 5 shows our results. The first two eigenvectors were chosen as our diffusion space basis vectors because as Fig. 5(inset) shows, those are the two dominant non-trivial eigenvalues in the spectrum and the rest go to zero as the number of data points are increased. Projecting the states onto this two-dimensional diffusion space, we see that the states all fall on a curve in this

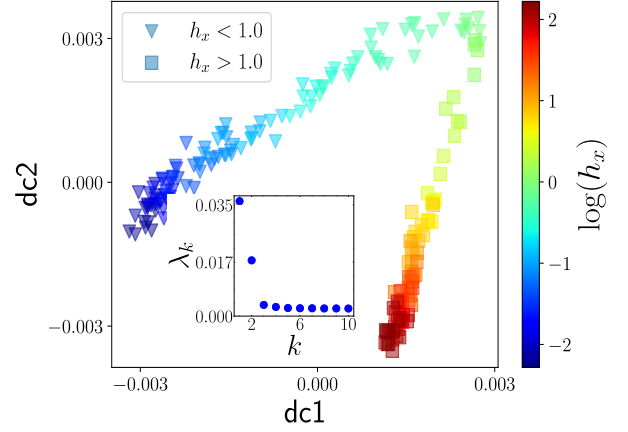


FIG. 5: The figure above shows phase identification from our dynamics data. The eigenvalue spectrum (inset) obtained from diffusion maps shows the two largest eigenvalues corresponding to the two dominant diffusion coordinates $dc1$ and $dc2$ (the trivial point $k = 0$, is not shown). The TACS data points largely fall on a curve parameterized by h_x in this 2D reduced diffusion space. The region near the critical point ($h_x = 1$) coincides with the inflection point region (green) of the curve, with points on either side belonging to the two different phases.

hyperplane along which the value of h_x increases monotonically, and the inflection point of the curve coincides with the quantum critical region. Therefore, it is apparent that the unsupervised learning algorithm was able to infer two phases from the data. In contrast to our ground state study, we were not able to map the diffusion coordinates to the phase-defining observables.

In a microcanonical ensemble, entropy functions as the thermodynamic potential and thus characterizes the phase transitions. The quantum critical region features the interplay of thermal and quantum fluctuations leading to the entropy being maximized [47, 50]. To calculate the 2^{nd} Renyi entropy, we first compute the purity using eqn 10 as follows

$$\begin{aligned} \gamma[\rho] &= \text{Tr}[\rho^2] \\ &\approx \frac{1}{N^2} \sum_{n \neq n'=1}^N \text{Tr}[\sigma_1^{(n)} \sigma_1^{(n')}] \times \dots \times \text{Tr}[\sigma_L^{(n)} \sigma_L^{(n')}] \end{aligned} \quad (19)$$

then $S_2 = -\log_2 \gamma$. The Renyi entropy has the same limits as the von Neumann entropy- it vanishes for pure states and reaches N for the maximally mixed state.

Figure 6 presents the entropy as calculated from TACS shots on a 10 qubit system using exact diagonalization. We use Bayesian inference, as detailed in appendix C 1 (see also Ref. 51). The results show clear evidence that entropy is maximized in the quantum critical region around $h_x = 1$ as shown in Fig. 2 of [47]. Error

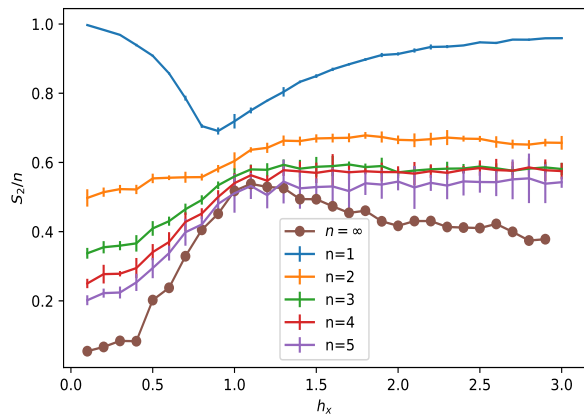


FIG. 6: The 2nd Renyi entropies for a 10-site 1DTFIM computed from TACS consisting of 100k shots. $n = \infty$ shows the Bayesian inference estimation for the thermodynamic limit and infinite TACS shots.

estimates for these values were obtained in Ref. 52, and given by:

$$N \geq \frac{4^{k+1}\gamma}{\epsilon^2\delta} \quad (21)$$

Where $1 - \delta$ is the probability of obtaining a good TACS dataset and ϵ is the additive error. For a $\delta = 0.33$ (67 percentile), and $N = 100,000$ shots, we find an additive error for the $n = 5$ entropy curve plotted in Fig. 6 at $h_x = 1.0$ of $S_2/n \approx 0.5 \pm 0.24$. This is larger than the observed error shown via error bars in Fig. 6 but only within a factor of order 1.

V. OUTLOOK

In this paper, we have identified an approach to studying quantum thermodynamics on a quantum computer in a way that is suitable for studying quantum materials and their phase diagrams. This approach consists of

- (i) preparing an initial state which equilibrates within the coherence time of the quantum computer,
- (ii) time evolving this state using a quantum algorithm to a randomly chosen time point t within some interval,
- (iii) extending shadow tomography methods to obtain a physically useful representation of the time-averaged density matrix, such as TACS used in this paper, and
- (iv) employing an unsupervised machine learning method to discover the phase diagram, with kernel methods such as diffusion maps showing promise.

Our approach parallels statistical mechanics calculations on classical Hamiltonians, where a random initial state is prepared, a Metropolis Monte-Carlo algorithm is run beginning from this state, and data is collected and analyzed using traditional observables and modern machine learning methods. Our results, demonstrating the existence of a quantum phase transition and the ability to map out regions of the phase diagram by a careful choice of initial conditions, show promise. Considering that we are just performing time evolution and measurements, our approach is simple compared to the existing methods [53–55] for studying thermodynamics on a quantum computer. The simplicity not only avoids the issues of optimizing a large number of parameters experienced by these methods but also allows us to exploit the advances in Hamiltonian dynamics. This leads to the possibility of studying thermodynamics on NISQ devices by using variational time evolution algorithms[56–58] such as the variational fast forwarding. These algorithms are relatively robust to errors and can simulate dynamics beyond the coherence time of quantum computers. Since TACS involve only single qubit rotations and computational basis measurements, an extension of our methods to quantum simulators also seems straightforward[59]. Lastly, it would be interesting to assess how this algorithm compares with finite temperature Quantum Monte-Carlo and at what system size the expected quantum advantage is reached.

Appendix A: Diagrammatic understanding of classical shadows

In this section, a diagrammatic understanding of the classical shadows will be developed. We'll work in the superoperator formalism where the indices of the density matrix ρ_{ij} are grouped together to make a vector $|\rho\rangle\rangle$ and the product $A\rho B$ translates to an operator $A \otimes B^T$ acting on the vector $|\rho\rangle\rangle$.

In general, we can view the outcomes obtained from many classical shadows measurements on the same prepared state ρ as defining an ensemble of states $S[\rho]$ where

$$S[\rho] = \sum_{b,x} P(b) \mathcal{P}_{b,x} \rho \mathcal{P}_{b,x} = \left[\sum_{b,x} P(b) \mathcal{P}_{b,x} \otimes \mathcal{P}_{b,x}^T \right] |\rho\rangle\rangle, \quad (A1)$$

and $\mathcal{P}_{b,x}$ is the projector in basis b onto qubit state $|x\rangle$.

To break this down into manageable parts, let's start from the one qubit case and work up to N qubits.

One qubit case. In the one qubit case, we have three bases $b \in \{X, Y, Z\}$ and choose to sample them uniformly i.e. $P(b) = 1/3$. We can thus express the one-qubit version of A1 with the diagram

$$S[\rho] = \frac{1}{3} \sum_{b,x} \text{---} \boxed{P_{bx}} \text{---} \boxed{\rho} \text{---} \boxed{P_{bx}} \text{---}. \quad (A2)$$

Using cap and cup, we can redraw this in the superoperator form:

$$S[\rho] = \frac{1}{3} \sum_{b,x} \text{Diagram} \quad (\text{A3})$$

We can view the highlighted box as a superoperator acting on the space of linear operators ρ . Remarkably, this particular superoperator consisting of a product of two projection operators simplifies substantially:

$$\sum_{b,x} \text{Diagram} = \left[\begin{array}{c} | \\ | \end{array} + \begin{array}{c} = \\ = \end{array} \right] \quad (\text{A4})$$

They amount to the sum of an identity and a cup-cap product. Using this simplification we recognize the one qubit case as the depolarizing map

$$S[\rho] = \frac{1}{3} \left[\text{Diagram} + \text{Diagram} \right] \quad (\text{A5})$$

where we further simplified using

$$\text{Diagram} = 1 \quad (\text{A6})$$

Inverting, we can extract the original density matrix (full tomography) via

$$\text{Diagram} = 3 \text{Diagram} - \text{Diagram} \quad (\text{A7})$$

Going from diagrammatic results to equations gives $S[\rho] = \frac{1}{3}(\rho + I)$ and $\rho = 3S[\rho] - I$, which is a single-qubit depolarizing channel.

Two-qubit case. In the two-qubit case, the CS map of Eq. A1 takes the form

$$\frac{1}{9} \sum_{b,x} \sum_{b',x'} \text{Diagram} \quad (\text{A8})$$

Again, we can add cups and caps to express it in superoperator form:

$$\text{Diagram} \quad (\text{A9})$$

This diagram shows that the one-qubit projection operators produce the same structure on each qubit as they did in the one-qubit case. Thus applying the same simplification as before we arrive at

$$\frac{1}{9} \left[\text{Diagram} + \text{Diagram} + \text{Diagram} + \text{Diagram} \right], \quad (\text{A10})$$

where again we used $\text{Tr}[\rho] = 1$. This expression amounts to a simple sum of all possible reduced density matrices.

We can invert our diagram for the two qubit case by first tracing over one of its qubits to get

$$\text{Diagram} = \frac{1}{3} \left[\text{Diagram} + \text{Diagram} \right]. \quad (\text{A11})$$

This allows us to rewrite the reduced density matrices in terms of the reduced density matrix of the classical shadow. Using this relation, we then arrive at the inverse

of the two-qubit classical shadow

$$(A12)$$

As for the one qubit case, we can convert our diagrams back to algebraic expressions. The results of this two-qubit case amount to the forward expression

$$S[\rho] = \frac{1}{9}(\rho + I \otimes \text{Tr}_1[\rho] + \text{Tr}_2[\rho] \otimes I + I \otimes I) \quad (A13)$$

and the inverse expression

$$\rho = 9S[\rho] - 3I \otimes \text{Tr}_1 S[\rho] - 3\text{Tr}_2 S[\rho] \otimes I + I \otimes I \quad (A14)$$

N-qubit case. The formulas we have derived for the one- and two-qubit cases readily extend to N -qubits. They are

$$S[\rho] = \frac{1}{3^L} \left(\rho + \sum_l \text{Tr}_l \rho + \sum_{l \neq l'} \text{Tr}_{ll'} \rho + \dots + I \right) \quad (A15)$$

for the forward map and for the inverse map

$$\rho = 3^L S[\rho] - 3^{L-1} \sum_l \text{Tr}_l S[\rho] + 3^{L-2} \sum_{l \neq l'} \text{Tr}_{ll'} S[\rho] + \dots + (-1)^L I, \quad (A16)$$

where we have suppressed the presence of identity operators that replace traced out regions for ease of notation. These expressions satisfy $\text{Tr}[\rho] = 1$ and $S[\rho] \geq 0$. The inverse map is not non-negative in general, but of course should be for the density matrices resulting from this map. Equation A16 may also be written as:

$$\rho = \frac{1}{N} \sum_{n=1}^N \bigotimes_{l=0}^L (3 |b_l^{(n)}; \sigma_l^{(n)}\rangle \langle b_l^{(n)}; \sigma_l^{(n)}| - 1), \quad (A17)$$

where l denotes the site-index and n denotes the shot-index.

Appendix B: Symmetries of 1DTFIM

1. \mathbb{Z}_2 symmetry

The 1DTFIM is invariant under global flipping of the z -component of the spin, the \mathbb{Z}_2 symmetry. This unitary symmetry can be expressed as

$$\mathcal{S} = \prod_i X_i. \quad (B1)$$

We can check that the symmetry operator \mathcal{S} commutes with the TFIM Hamiltonian i.e. $[\mathcal{S}, H_{TFIM}] = 0$. This allows us to write H_{TFIM} in block diagonal form with each block corresponding to eigenvalues 1 (even parity) and -1 (odd parity) of \mathcal{S} . States in these sectors evolve independently of each other. If we start in the GHZ state

$$|\text{Cat}\rangle = \frac{|00 \dots 0\rangle + |11 \dots 1\rangle}{\sqrt{2}}, \quad (B2)$$

a time reversal even state, we remain in the even sector under time evolution. Since the magnetization of this state is 0, the magnetization will stay at this value forever. Thus, equilibration of the order parameter is not an issue. Since the TFIM Hamiltonian is purely real, it is symmetric under complex conjugation \mathcal{K} , and consequently the eigenvalues are also real. Hence, it is also symmetric under $\mathcal{T} = \mathcal{S}\mathcal{K}$ i.e. time reversal symmetry.

2. Chiral symmetry

The 1DTFIM is also symmetric under the following chiral operator

$$\mathcal{C} = ZYZY \dots ZY \quad (B3)$$

We can check that \mathcal{C} anticommutes with H_{TFI} , so for every energy eigenstate E , there exists an eigenstate with $-E$, which makes the spectrum of 1DTFIM mirror symmetric about zero energy.

Appendix C: Parameter Learning from Ground State Data

The UL model we implemented was able to unveil the symmetry breaking phase transition of 1DTFIM from ground state CS data (Fig. 3(d)). It did so by generating diffusion coordinates which are directly correlated to relevant parameters, the order parameter M_z and the model parameter h_x of 1DTFIM. Fig. 7 shows the correlation between the diffusion coordinates and these parameters.

1. Bayesian Inference Extrapolation of Entropy Data

To infer the entropy in the limit of large N , the number of shots, and large n , the number of qubits, we need

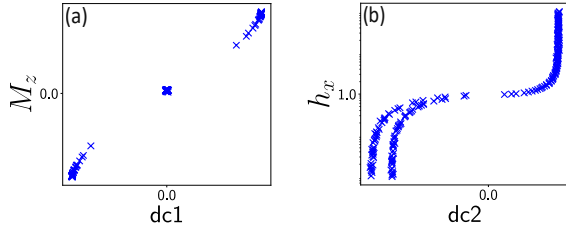


FIG. 7: Learning 1DTFIM model parameter and order parameter from CS data. Direct correlation between (a) dc1 and order parameter M_z and (b) dc2 and model parameter h_x .

to extrapolate the estimate we obtain from CS data. At first glance, this would seem hard to do because the error in our estimates grows exponentially with the locality of the observables and entropy is not a local observable. However, the dynamics data we have obtained represents a mixed state with volume-law entanglement and, due to the finite energy—the microcanonical stand-in for temperature—typically has exponentially decaying correlations beyond a correlation length. Hence, we expect the entropy of the reduced density matrix of a region A with n_A qubits will obey $S \propto n_A$ even for small n_A . Our approach to extrapolate the entropy is therefore to build a probability model $p(X|\theta)$ with parameters θ that captures our estimated entropy value data X .

To simplify the calculation of entropy, we will compute the second Renyi entropy of a sub-region A : $S_A = -\log_2 \gamma_A$, $\gamma = \text{Tr} \rho_A^2$. To obtain a model of this entropy as a function of the number of CS shots N and qubits n_A , a data set of values Y given by the entropy S_A and dependent variables X given by (N, n_A) , we generated data from the maximally mixed state $\rho = (1/d)I$, $d = 2^{n_A}$ the size of the Hilbert space. The result fit a model of the form (see Fig. 8):

$$\gamma(n, N) = ae^{-bn} + ce^{dn}/N, \quad \sigma_\gamma = ee^{fn} \quad (\text{C1})$$

with positive parameters a, b, c, d, e, f . Namely, we found the purity γ is linear in $1/N$ but exponential in n .

Given the mean and variance as modeled above, we can then model the probability distribution from which a given data point $(\vec{x}, y) \in (X, Y)$ is a sample as a Gaussian:

$$P(y|\theta, \vec{x}) = \frac{1}{\sqrt{2\pi\sigma^2(\vec{x}; \theta)}} e^{-(y - \mu(\vec{x}; \theta))^2 / 2\sigma^2(\vec{x}; \theta)}. \quad (\text{C2})$$

Then by Bayes Law we can learn the posterior

$$p(\theta \setminus Y, X) = \frac{\prod_{(\vec{x}, y) \in (X, Y)} P(y|\theta, \vec{x}) P(\theta)}{P(Y \setminus X)} \quad (\text{C3})$$

where $P(X, Y) = \int d\theta \prod_{(X, Y)} P(\vec{x}, y|\theta) P(\theta)$ is called the evidence that provides a sense of how well the model is performing.

The probability of observing a new data point (\vec{x}', y') is then given by the posterior predictive

$$P(\vec{x}', y' \setminus X, Y) = \int d\theta p(\vec{x}', y'|\theta) P(\theta \setminus X, Y) \quad (\text{C4})$$

An estimate of which is obtainable from a set of samples Θ drawn from $P(\theta \setminus X, Y)$

$$P(\vec{x}', y' \setminus X, Y) = \frac{1}{|\Theta|} \sum_{\theta \in \Theta} p(\vec{x}', y'|\theta) \quad (\text{C5})$$

We are then specifically interested in the mean and standard deviation of $P((\infty, \infty), y \setminus X, Y)$. Knowing this, we solve the problem of extrapolating the entropy from a finite number of shots and qubits for the entropy is the mean and our uncertainty in obtaining it is the standard deviation.

It remains then to obtain samples from the posterior $P(\theta \setminus X, Y)$. We could do so using a straightforward Monte Carlo algorithm. For example, starting with an initial choice for the parameters θ_0 , we pick a random direction in parameter space and move an amount δ in that direction to obtain θ_{trial} . We then compute

$$\begin{aligned} \log(r) = \log \frac{P(\theta_{\text{trial}} \setminus X, Y)}{P(\theta_0 \setminus X, Y)} = \\ \sum_{(\vec{x}, y) \in (X, Y)} (\log P(\vec{x}, y|\theta_{\text{trial}}) - \log P(\vec{x}, y|\theta_0)) + \\ \log P(\theta_{\text{trial}}) - \log P(\theta_0) \end{aligned} \quad (\text{C6})$$

which simplifies if we choose a uniform distribution for $P(\theta)$. We keep the trial, setting $\theta_1 = \theta_{\text{trial}}$ if a random number q between 0 and 1 satisfies $q < r$ and reject otherwise. Either way, we repeat the process generating ultimately a list Θ of correlated samples θ_i from which we can estimate the entropy and uncertainty from $P((\infty, \infty), y \setminus X, Y)$.

However, a better approach than the Metropolis algorithm is to instead use the NUTS algorithm available in PyMC. This algorithm automatically chooses parameters in hamiltonian monte-carlo (HMC) and is more efficient than Metropolis for Bayesian inference. See Ref. 60.

[1] Yudong Cao, Jonathan Romero, Jonathan P. Olson, Matthias Degroote, Peter D. Johnson, Mária Kieferová, Ian D. Kivlichan, Tim Menke, Borja Peropadre, Nicolas

P. D. Sawaya, Sukin Sim, Libor Veis, and Alán Aspuru-Guzik. Quantum chemistry in the age of quantum computing. *Chemical Reviews*, 119(19):10856–10915, 10

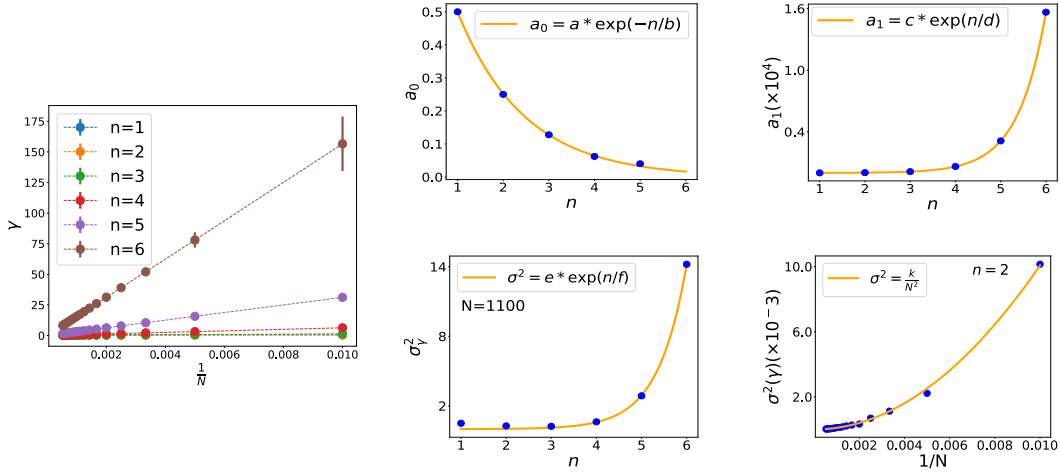


FIG. 8: Developing a model for purity γ as a normal distribution. (a) μ_γ is linear in $\frac{1}{N}$, so let's say: $\mu_\gamma = a_0 + \frac{a_1}{N}$. (b) The intercept a_0 can be modeled as an inverse exponential function of n , and (c) the slope a_1 as exponential in n . (d), (e) show that the variance σ^2 can be closely approximated by an exponential function in n and linear in $\frac{1}{N^2}$.

- 2019.
- [2] Dave Wecker, Matthew B. Hastings, Nathan Wiebe, Bryan K. Clark, Chetan Nayak, and Matthias Troyer. Solving strongly correlated electron models on a quantum computer. *Phys. Rev. A*, 92:062318, Dec 2015.
- [3] He Ma, Marco Govoni, and Giulia Galli. Quantum simulations of materials on near-term quantum computers. *npj Computational Materials*, 6(1):85, 2020.
- [4] Nagaosa Naoto. Superconductivity and antiferromagnetism in high- T_c cuprates. *Science*, 275(5303):1078–1079, 1997.
- [5] Xingjiang Zhou, Wei-Sheng Lee, Masatoshi Imada, Nandini Trivedi, Philip Phillips, Hae-Young Kee, Päivi Törmä, and Mikhail Erements. High-temperature superconductivity. *Nature Reviews Physics*, 3(7):462–465, 2021.
- [6] John McGreevy. In pursuit of a nameless metal, Oct 2010.
- [7] R. B. Laughlin. Nobel lecture: Fractional quantization. *Rev. Mod. Phys.*, 71:863–874, Jul 1999.
- [8] Lucile Savary and Leon Balents. Quantum spin liquids: a review. *Reports on Progress in Physics*, 80(1):016502, nov 2016.
- [9] Steven R. White. Density matrix formulation for quantum renormalization groups. *Phys. Rev. Lett.*, 69:2863–2866, Nov 1992.
- [10] Steven R. White. Density-matrix algorithms for quantum renormalization groups. *Phys. Rev. B*, 48:10345–10356, Oct 1993.
- [11] Ulrich Schollwöck. The density-matrix renormalization group in the age of matrix product states. *Annals of Physics*, 326(1):96–192, 2011. January 2011 Special Issue.
- [12] Federico Becca and Sandro Sorella. *Quantum Monte Carlo Approaches for Correlated Systems*. Cambridge University Press, 2017.
- [13] Antoine Georges, Gabriel Kotliar, Werner Krauth, and Marcelo J. Rozenberg. Dynamical mean-field theory of strongly correlated fermion systems and the limit of infinite dimensions. *Rev. Mod. Phys.*, 68:13–125, Jan 1996.
- [14] Richard P. Feynman. Simulating physics with computers. *International Journal of Theoretical Physics*, 21(6):467–488, 1982.
- [15] Bryan O’Gorman, Sandy Irani, James Whitfield, and Bill Fefferman. Electronic structure in a fixed basis is qma-complete, 2021.
- [16] Sevag Gharibian and Justin Yirka. The complexity of simulating local measurements on quantum systems. *Quantum*, 3:189, September 2019.
- [17] Adam D. Bookatz. Qma-complete problems. *Quantum Info. Comput.*, 14:361–383, apr 2014.
- [18] Julia Kempe, Alexei Kitaev, and Oded Regev. The complexity of the local hamiltonian problem. In Kamal Lodaya and Meena Mahajan, editors, *FSTTCS 2004: Foundations of Software Technology and Theoretical Computer Science*, pages 372–383, Berlin, Heidelberg, 2005. Springer Berlin Heidelberg.
- [19] Maria Laura Baez, Marcel Goihl, Jonas Haferkamp, Juan Bermejo-Vega, Marek Gluza, and Jens Eisert. Dynamical structure factors of dynamical quantum simulators. *Proceedings of the National Academy of Sciences*, 117(42):26123–26134, Oct 2020.
- [20] Alessandro Rudi, Leonard Wossnig, Carlo Ciliberto, Andrea Rocchetto, Massimiliano Pontil, and Simone Severini. Approximating hamiltonian dynamics with the nyström method. *Quantum*, 4:234, Feb 2020.
- [21] Scott Aaronson. Shadow tomography of quantum states. In *Proceedings of the 50th Annual ACM SIGACT Symposium on Theory of Computing*, STOC 2018, page 325–338, New York, NY, USA, 2018. Association for Computing Machinery.
- [22] Hsin-Yuan Huang, Richard Kueng, and John Preskill. Predicting many properties of a quantum system from very few measurements. *Nature Physics*, 16(10):1050–1057, Jun 2020.
- [23] Hsin-Yuan Huang, Richard Kueng, Giacomo Torlai, Victor V Albert, and John Preskill. Provably efficient machine learning for quantum many-body problems. *arXiv preprint arXiv:2106.12627*, 2021.

- [24] Hsin-Yuan Huang, Sitan Chen, and John Preskill. Learning to predict arbitrary quantum processes, 2022.
- [25] James P. Sethna. *Statistical mechanics: Entropy, order parameters, and complexity*, page 79–85. Oxford University Press, 2012.
- [26] John von Neumann. Proof of the ergodic theorem and the h-theorem in quantum mechanics. *The European Physical Journal H*, 35(2):201–237, 2010.
- [27] Christian Gogolin and Jens Eisert. Equilibration, thermalisation, and the emergence of statistical mechanics in closed quantum systems. *Reports on Progress in Physics*, 79(5):056001, apr 2016.
- [28] Noah Linden, Sandu Popescu, Anthony J. Short, and Andreas Winter. Quantum mechanical evolution towards thermal equilibrium. *Phys. Rev. E*, 79:061103, Jun 2009.
- [29] Peter Reimann and Michael Kastner. Equilibration of isolated macroscopic quantum systems. *New Journal of Physics*, 14(4):043020, apr 2012.
- [30] Luis Pedro García-Pintos, Noah Linden, Artur S. L. Malabarba, Anthony J. Short, and Andreas Winter. Equilibration time scales of physically relevant observables. *Phys. Rev. X*, 7:031027, Aug 2017.
- [31] Ronald R Coifman and Stéphane Lafon. Diffusion maps. *Applied and computational harmonic analysis*, 21(1):5–30, 2006.
- [32] J De la Porte, BM Herbst, W Hereman, and SJ Van Der Walt. An introduction to diffusion maps. In *Proceedings of the 19th symposium of the pattern recognition association of South Africa (PRASA 2008)*, Cape Town, South Africa, pages 15–25, 2008.
- [33] Andreas Elben, Steven T. Flammia, Hsin-Yuan Huang, Richard Kueng, John Preskill, Benoît Vermersch, and Peter Zoller. The randomized measurement toolbox, 2022.
- [34] E. Knill. Quantum computing with realistically noisy devices. *Nature*, 434(7029):39–44, mar 2005.
- [35] Michael A. Nielsen and Isaac L. Chuang. *Quantum Computation and Quantum Information: 10th Anniversary Edition*. Cambridge University Press, 2010.
- [36] Sheldon Goldstein, Joel L Lebowitz, Christian Mastrodonato, Roderich Tumulka, and Nino Zanghì. Normal typicality and von neumann’s quantum ergodic theorem. *Proceedings of the Royal Society A: Mathematical, Physical and Engineering Sciences*, 466(2123):3203–3224, 2010.
- [37] Anthony J Short and Terence C Farrelly. Quantum equilibration in finite time. *New Journal of Physics*, 14(1):013063, jan 2012.
- [38] Norman Margolus. Counting distinct states in physical dynamics. *arXiv preprint arXiv:2111.00297*, 2021.
- [39] Matthew Fishman, Steven R. White, and E. Miles Stoudenmire. The ITensor software library for tensor network calculations, 2020.
- [40] Hsin-Yuan Huang and Richard Kueng. Predicting features of quantum systems from very few measurements, 2019.
- [41] John Preskill. Quantum Computing in the NISQ era and beyond. *Quantum*, 2:79, August 2018.
- [42] Giuseppe Carleo, Ignacio Cirac, Kyle Cranmer, Laurent Daudet, Maria Schuld, Naftali Tishby, Leslie Vogt-Maranto, and Lenka Zdeborová. Machine learning and the physical sciences. *Reviews of Modern Physics*, 91(4):045002, 2019.
- [43] Joaquin F Rodriguez-Nieva and Mathias S Scheurer. Identifying topological order through unsupervised machine learning. *Nature Physics*, 15(8):790–795, 2019.
- [44] Alexander Lidiak and Zhexuan Gong. Unsupervised machine learning of quantum phase transitions using diffusion maps. *Physical Review Letters*, 125(22):225701, 2020.
- [45] Ingwer Borg and Patrick JF Groenen. *Modern multi-dimensional scaling: Theory and applications*. Springer Science & Business Media, 2005.
- [46] Subir Sachdev. *Quantum Phase Transitions*. Cambridge University Press, 2 edition, 2011.
- [47] Jianda Wu, Lijun Zhu, and Qimiao Si. Crossovers and critical scaling in the one-dimensional transverse-field ising model. *Physical Review B*, 97(24):245127, 2018.
- [48] Jutho Haegeman, Christian Lubich, Ivan Oseledets, Bart Vandereycken, and Frank Verstraete. Unifying time evolution and optimization with matrix product states. *Phys. Rev. B*, 94:165116, Oct 2016.
- [49] <https://github.com/orialb/TimeEvoMPS.jl>.
- [50] Jianda Wu, Lijun Zhu, and Qimiao Si. Entropy accumulation near quantum critical points: effects beyond hyperscaling. *Journal of Physics: Conference Series*, 273(1):012019, jan 2011.
- [51] Joseph M Lukens, Kody JH Law, and Ryan S Bennink. A bayesian analysis of classical shadows. *npj Quantum Information*, 7(1):1–10, 2021.
- [52] Stefan H. Sack, Raimel A. Medina, Alexios A. Michailidis, Richard Kueng, and Maksym Serbyn. Avoiding barren plateaus using classical shadows. *PRX Quantum*, 3:020365, Jun 2022.
- [53] Luuk Coopmans, Yuta Kikuchi, and Marcello Benedetti. Predicting gibbs state expectation values with pure thermal shadows, 2022.
- [54] Mario Motta, Chong Sun, Adrian T. K. Tan, Matthew J. O’Rourke, Erika Ye, Austin J. Minnich, Fernando G. S. L. Brandão, and Garnet Kin-Lic Chan. Determining eigenstates and thermal states on a quantum computer using quantum imaginary time evolution. *Nature Physics*, 16(2):205–210, 2020.
- [55] Akhil Francis, Daiwei Zhu, Cinthia Huerta Alderete, Sonika Johri, Xiao Xiao, James K. Freericks, Christopher Monroe, Norbert M. Linke, and Alexander F. Kemper. Many-body thermodynamics on quantum computers via partition function zeros. *Science Advances*, 7(34):eabf2447, 2021.
- [56] Yong-Xin Yao, Niladri Gomes, Feng Zhang, Cai-Zhuang Wang, Kai-Ming Ho, Thomas Iadecola, and Peter P. Orth. Adaptive variational quantum dynamics simulations. *PRX Quantum*, 2:030307, Jul 2021.
- [57] Xiao Yuan, Suguru Endo, Qi Zhao, Ying Li, and Simon C. Benjamin. Theory of variational quantum simulation. *Quantum*, 3:191, oct 2019.
- [58] Cristina Cîrstoiu, Zoë Holmes, Joseph Iosue, Lukasz Cincio, Patrick J. Coles, and Andrew Sornborger. Variational fast forwarding for quantum simulation beyond the coherence time. *npj Quantum Information*, 6(1):82, 2020.
- [59] Hannes Bernien, Sylvain Schwartz, Alexander Keesling, Harry Levine, Ahmed Omran, Hannes Pichler, Soonwon Choi, Alexander S. Zibrov, Manuel Endres, Markus Greiner, Vladan Vuletić, and Mikhail D. Lukin. Probing many-body dynamics on a 51-atom quantum simulator. *Nature*, 551(7682):579–584, 2017.
- [60] John Salvatier, Thomas V Wiecki, and Christopher Fonnesbeck. Probabilistic programming in python using pymc3. *PeerJ Computer Science*, 2:e55, 2016.